Monatshefte für Chemie 133, 889–908 (2002)

Monatshefte für Chemie
Chemical Monthly

Vibrational Spectroscopy and Analytical Electron Microscopy Studies of Fe–V–O and In–V–O Thin Films

Angela Šurca Vuk[1], **Boris Orel**[1,*], **Goran Dražič**[2], and **Philippe Colomban**[3]

[1] National Institute of Chemistry, SL-1000 Ljubljana, Slovenia
[2] Josef Stefan Institute, SL-1000 Ljubljana, Slovenia
[3] Laboratoire de Dynamique, Interactions et Reactivite, Centre National de la Recherche Scientifique – Universite Pierre et Marie Curie, F-94320 Thiais, France

Summary. Orthovanadate ($M^{3+}VO_4$; M = Fe, In) and vanadate ($Fe_2V_4O_{13}$) thin films were prepared using sol-gel synthesis and dip coating deposition. Using analytical electron microscopy (AEM), the chemical composition and the degree of crystallization of the phases present in the thin Fe–V–O films were investigated. TEM samples were prepared in both orientations: parallel (plan view) and perpendicular (cross section) to the substrate. In the first stages of crystallization, when the particle sizes were in the nanometer range, the classical identification of phases using electron diffraction was not possible. Instead of measuring d values, experimentally selected area electron diffraction (SAED) patterns were compared to calculated (simulated) patterns in order to determine the phase composition. The problems of evaluating the ratio of amorphous and crystalline phases in thin films are reported.

Results of TEM and XRD as well as IR and *Raman* spectroscopy showed that the films made at lower temperatures (300°C) consisted of nanograins embedded in the dominating amorphous phase. Characteristic vibrational spectra allowed to distinguish between the different crystalline phases, since the IR and *Raman* bands showed broadening due to the decreasing particle size of the films thermally treated at lower temperatures. Vibrational analysis also showed that the electrochemical cycling of crystalline films led to spectra that were in close agreement with the spectra of the nanocrystalline films prepared at lower temperatures. The formation of a nanocrystalline structure is therefore a prerequisite for obtaining a higher charging/discharging stability of Fe–V–O and In–V–O films.

Keywords. Vanadates; Thin films; Sol-gel; Electrochromism; IR spectroscopy; Electron microscopy.

Introduction

The electrochromic properties of transition metal orthovanadates ($M^{3+}VO_4$, M = Ce, Fe, In, ...) have been extensively studied because of their potential for use as cathode materials in lithium rocking chair batteries [1–3]. Relatively little work

* Corresponding author. E-mail: boris.orel@ki.si

has been carried out on thin films of these materials, despite the fact that they exhibit electrochromism [4–6]. One of the most attractive properties of the electrochromic orthovanadates is their low optical response (below 20% T) during the insertion of Li^+ ions and electrons together with a high charge insertion/extraction capacity which makes it possible to use these films in electrochromic devices in combination with electrochromically active WO_3 or Nb_2O_5 [7].

Electrochemical studies revealed that amorphous V_2O_5 powders exhibit long-term cycling stability (> 1000 cycles), better than that observed for the corresponding crystalline V_2O_5 powders [8]. In our recent studies of In–V–O and Fe–V–O films we have shown that sol-gel synthesis permitted the production of films which exhibited, after different thermal treatments, amorphous, nanocrystalline, or well-defined crystalline structures [9–14]. One of the aims of this study is to show, by means of vibrational spectroscopy, correlations between the structure of In–V–O and Fe–V–O films prepared at low temperatures (300°C) and the structure that the initially crystalline $InVO_4$, $FeVO_4$, and $Fe_2V_4O_{13}$ films obtain after electrochemical cycling.

In addition to vibrational spectroscopy, analytical electron microscopy was also used. Due to its lateral and spatial resolution it is one of the most effective methods for studying thin films of various thicknesses and compositions. Using energy-dispersive X-ray spectroscopy (EDXS), electron diffraction, and dark-field imaging, crystalline phases with grain sizes down to a few nanometers can be characterized. Problems arise, however, when the crystal size of the phases is even smaller, *i.e.* in the region where the nanocrystalline phase is formed from the amorphous phase. The usually accepted definition [15] of an amorphous material is one for which the locations of the neighbouring atoms are defined by a probability function with probabilities lower than unity. In an amorphous material the electron scattering from areas as large as 1.5 nm can be coherent [16, 17]. The consequence of coherent scattering is that the selected area electron diffraction (SAED) patterns consist of diffuse rings (haloes), whereas in dark-field images spots with bright contrast are present. It is characteristic of the technique that the size of the bright spots increases with increasing defocus. In the case of a nanocrystalline material, the rings in SAED patterns are sharper and more complex; in dark-field images, the bright crystallites are well resolved. The identification of phases from electron diffraction patterns of nanocrystalline samples is often problematic due to the diffuse rings. In the present work we report on the identification of nanocrystalline phases in thin Fe–V–O films using a comparison of experimental and the simulated SAED patterns.

Results and Discussion

Analytical electron microscopy of films

Simulated electron diffraction 'powder' patterns were calculated using the EMS program package (Electron Microscopy Simulation program from Dr. *P. Stadelmann*, EPFL-CIME, Lausanne, Switzerland) [18]. As a result, a listing of the positions of the powder lines and the intensity of the lines was created. Intensities were calculated from the structure factors and corrected by a shape factor depending on the crystal

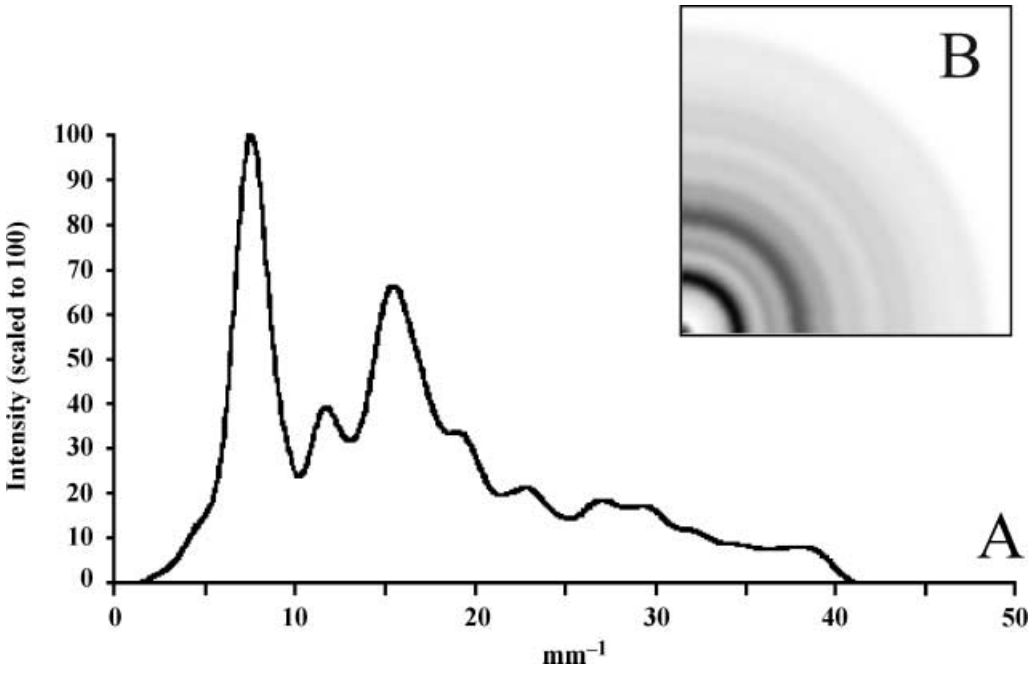

Fig. 1. A) Calculated distribution of intensities; B) their graphical representation for a triclinic $FeVO_4$ with 1 nm crystal size at 200 keV beam energy and 980 mm camera length

size. Dynamic effects were not considered in the calculations. To be able to compare the experimental and the simulated electron diffraction patterns, images were constructed from the intensity distributions. To determine the compounds present in the thin films we systematically calculated electron diffraction patterns for all possible phases for a mean crystallite size between 0.5 and 5 nm. For the simulations we used published crystal structure data for $Fe_2V_4O_{13}$ [19], $FeVO_4$ [20], $FeVO_4$-II (high-pressure form) [21], $InVO_4$-I [22], $InVO_4$-III [23], Fe_2O_3 [24], and V_2O_5 [25].

An example of a calculated intensity distribution for a triclinic $FeVO_4$ phase [20] with a crystal size of 1 nm and a corresponding simulated electron diffraction pattern are shown in Fig. 1. In this compound, three independent iron atoms are joined in a doubly bent chain of six edge-sharing iron polyhedra [20]. Two iron atoms are in a distorted octahedral and one in a distorted trigonal bipyramidal environment. The chains of iron polyhedra are joined by VO_4 tetrahedra which share corners with up to four iron polyhedra within a single chain.

A series of simulated patterns for a monoclinic $Fe_2V_4O_{13}$ phase [19] where the crystal size varied from 0.5 to 5 nm is depicted in Fig. 2. From very diffuse haloes in the pattern for 0.5 nm, which are characteristic for amorphous materials, the rings become sharper and more complicated with increasing crystal size. The $Fe_2V_4O_{13}$ crystal structure [19] consists of Fe^{3+} octahedra and V^{5+} tetrahedra. Iron-distorted octahedra form dimeric Fe_2O_{10} units, whereas four VO_4 tetrahedra are linked through corners in a U-shaped $(V_4O_{13})^{6-}$ polyanion. Each Fe_2O_{10} unit shares its oxygens with seven different V_4O_{13} groups. Such an arrangement creates hexagonal and narrow tetragonal empty tunnels.

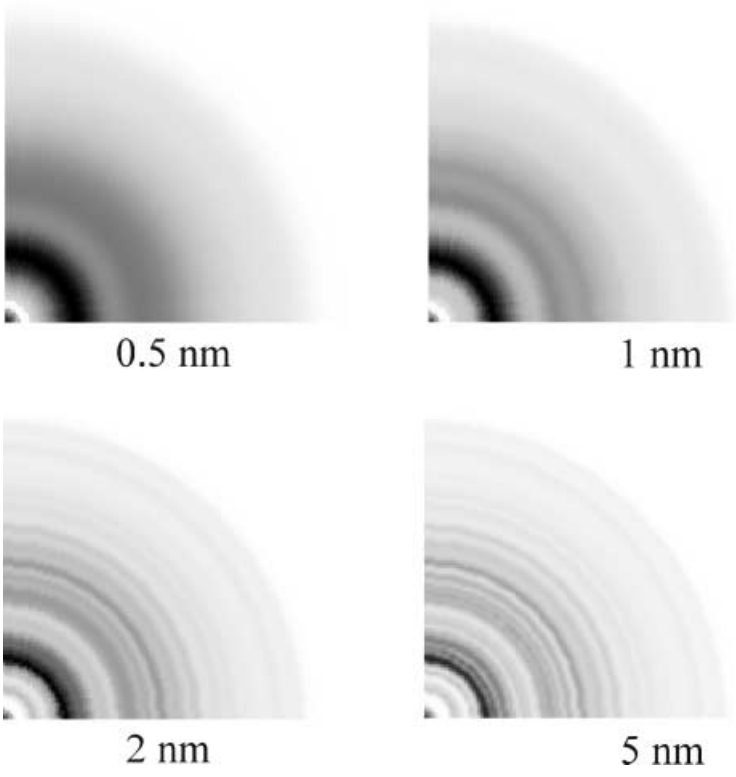

Fig. 2. Simulated SAED patterns (one quarter shown) of a monoclinic $Fe_2V_4O_{13}$ phase using crystal sizes of 0.5, 1, 2, and 5 nm

A central dark-field (CDF) TEM micrograph of a sample with the composition Fe:V = 1:2 (300°C) is displayed in Fig. 3 together with a comparison of the experimental and simulated SAED pattern. The white spots in the micrograph have a dimension of about 1 nm (the picture was collected very close to *Gauss*'s focus), and the SAED pattern was found to be quite diffuse; nevertheless, several circles of various intensity could still be resolved. The main question was: is the sample composed of just an amorphous phase or are there some crystalline phases present? The experimental diffraction pattern was compared to simulated patterns, and the best match was found in the case of the high-pressure orthorhombic form of iron vanadate ($FeVO_4$-II [21]) with a crystallite size of 1 nm (Fig. 3B). The structural features of $FeVO_4$-II [21] are one-dimensional chains of edge-sharing FeO_6 octahedra running along the *c* axis. The chains are linked through VO_4 tetrahedra.

In a thin film sample with the composition Fe:V = 1:1, which was thermally treated at 300°C, we found very similar SAED patterns but with sharper circles (Fig. 4B). In a dark-field TEM micrograph, bright areas with sizes of 5 nm and more were found (Fig. 4A). In this case the presence of nanocrystals was evident. The best match between the experimental and the simulated SAED patterns was found for the orthorhombic $FeVO_4$-II phase [21] with 5 nm particle size (Fig. 4B). Based on the similarities of the diffraction patterns and good agreement between the experimental patterns and the simulated ones we concluded that the crystalline phase was also present in the sample shown in Fig. 3 (nanometer-sized particles of

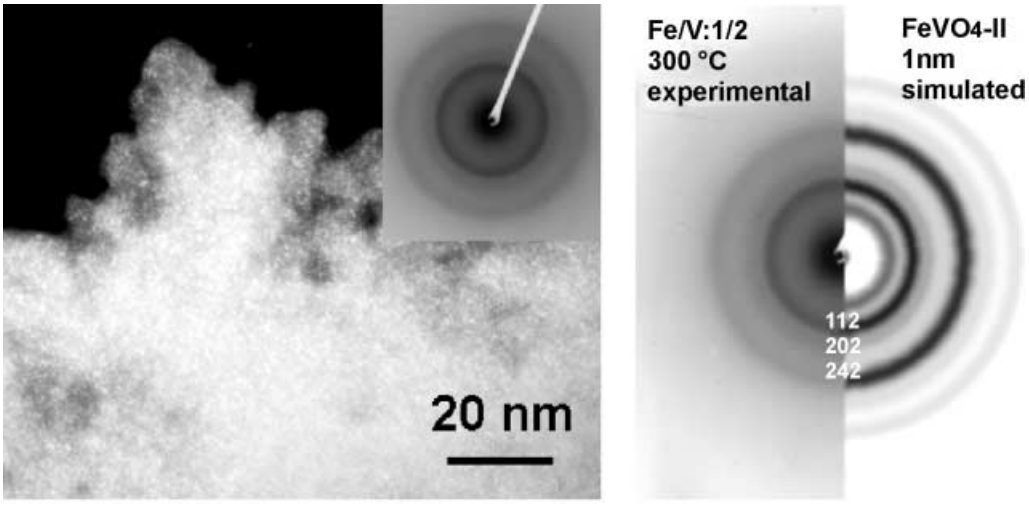

Fig. 3. A) Dark-field TEM micrograph (plan view) of a thin film with a molar ratio Fe:V = 1:2 thermally treated at 300°C; B) comparison of experimental and calculated SAED patterns for an orthorhombic $FeVO_4$-II phase

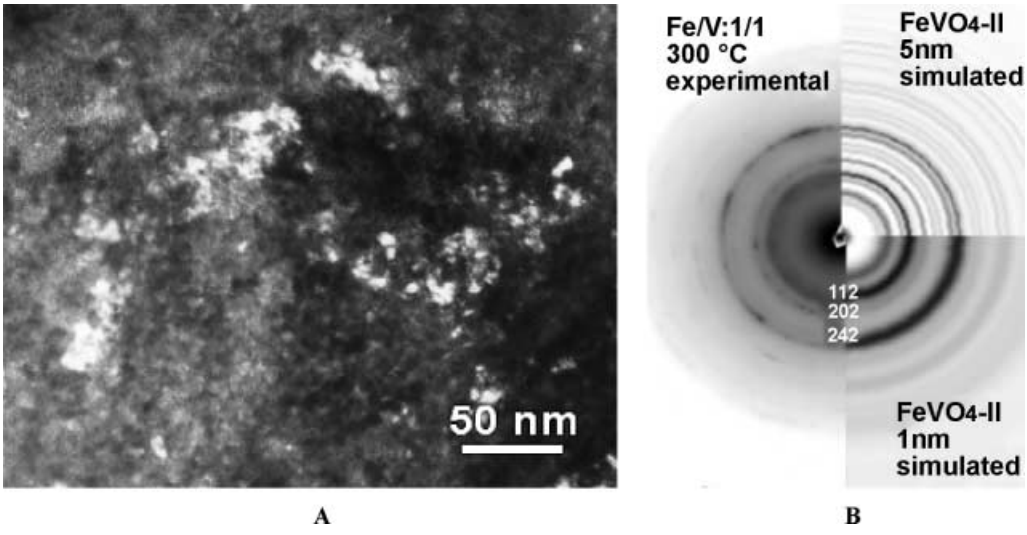

Fig. 4. A) Dark-field TEM micrograph (plan view) of a thin film with a molar ratio Fe:V = 1:1 thermally treated at 300°C; B) comparison of experimental and calculated SAED patterns for an orthorhombic $FeVO_4$-II phase

orthorhombic $FeVO_4$-II). This conclusion was in agreement with the results obtained with IR spectroscopy (see below).

In Fig. 5, the central dark-field (CDF) TEM micrograph and SAED pattern of a cross-section of a Fe:V = 1:2 (400°C) thin film are shown. The estimated film thickness was close to 150 nm. Two types of crystallites were found, one with a size around 50 nm and the other with a size below 5 nm. A bimodal distribution of

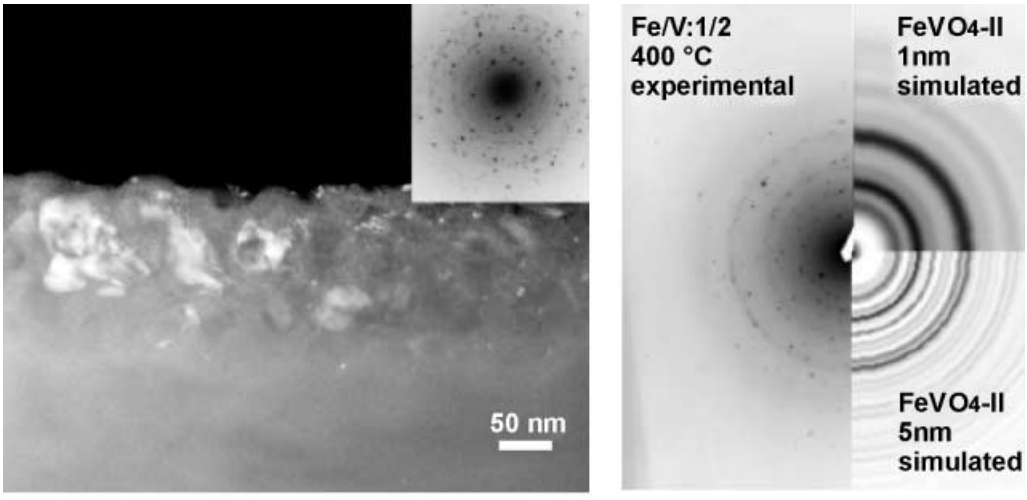

Fig. 5. A) Dark-field TEM micrograph (cross section) of a thin film with a molar ratio Fe:V = 1:2 thermally treated at 400°C; B) comparison of experimental and calculated SAED patterns for a $FeVO_4$-II phase

the crystallite sizes could be seen in the SAED patterns, which besides distinctive spots also showed faint uniform rings. An EDXS analysis performed on various points on the thin film indicated the presence of Fe and V in an approximate ratio of 1:2. All spots from the SAED patterns could be indicated for the monoclinic $Fe_2V_4O_{13}$ phase [19]; so it was concluded that the larger grains in Fig. 5A consist of this phase. Based on the comparison of the experimental and the simulated SAED patterns (Fig. 5B) we found that the faint rings suggest the presence of the fine-grained (around 5 nm) orthorhombic $FeVO_4$-II phase. A TEM micrograph of the Fe:V = 1:1 film prepared at 500°C revealed grains with dimensions between 50 and 80 nm corresponding to the monoclinic $FeVO_4$ phase. These grains were randomly oriented, and EDXS showed that the chemical composition in the film was uniform.

In all cases (Figs. 3–5), the presence of an amorphous phase in the thin film could not be excluded. The usual method in conventional transmission electron microscopy for determining the presence of an amorphous phase in samples in which the major constituents are crystalline is a dark-field imaging using diffusely scattered electrons [15]. In the case of fine-grained polycrystalline samples this method is not effective because of the presence of circles in diffraction patterns. Insome cases, high-resolution electron microscopy (HRTEM) can provide the answer; however, the limitations are sample thickness, sample preparation, and microscope resolution. During the preparation of TEM samples the thinnest areas, where the HRTEM approach is effective, are most likely to have a damaged structure.

For comparison, the XRD spectra of the vanadate films prepared at the highest temperatures ($FeVO_4$ and $InVO_4$ at 500°C, $Fe_2V_4O_{13}$ at 400°C) are shown in Fig. 6. The XRD spectra revealed the most intense bands of the corresponding phases: for the films with the molar ratio Fe:V = 1:2 the monoclinic $Fe_2V_4O_{13}$ phase (JCPDS 39-08930) and for films with Fe:V = 1:1 the triclinic $FeVO_4$ phase (JCPDS

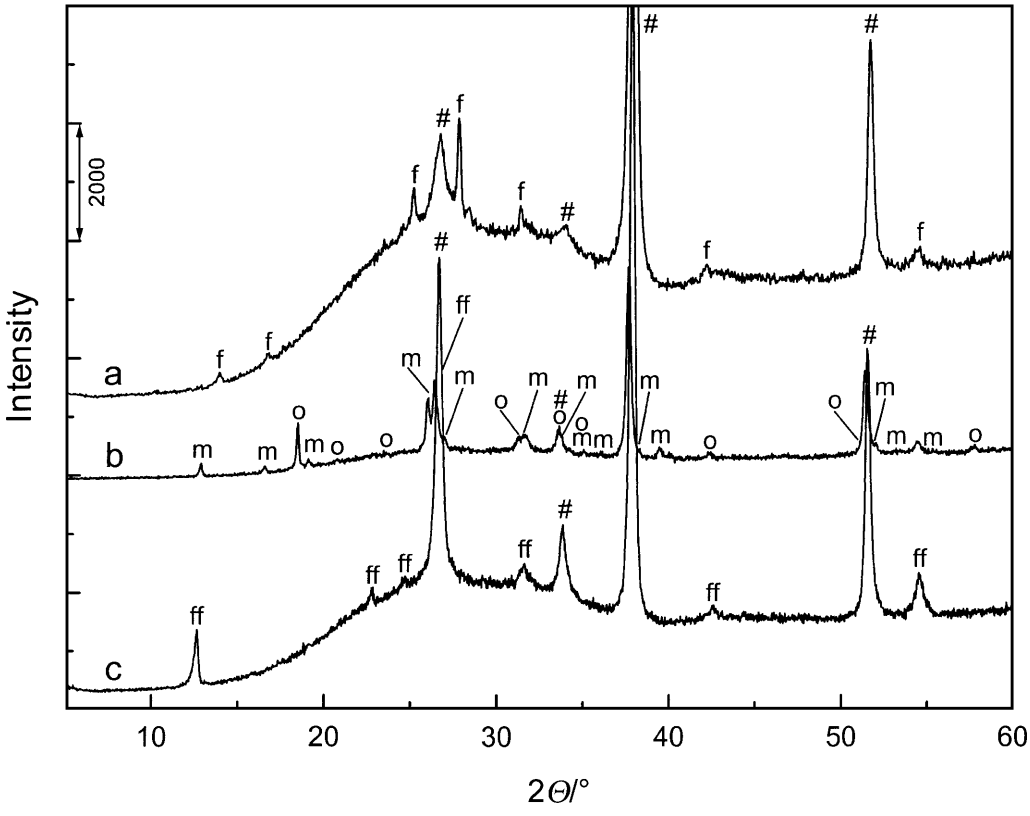

Fig. 6. XRD spectra of thin vanadate films: a) $FeVO_4$ (500°C), b) $InVO_4$ (500°C), c) $Fe_2V_4O_{13}$ (400°C); *f* denotes triclinic $FeVO_4$ phase, *ff* monoclinic $Fe_2V_4O_{13}$ phase, *m* monoclinic $InVO_4$-I phase, *o* orthorhombic $InVO_4$-III phase, and # diffraction peaks of the SnO_2/F glass substrates

38-1372). The XRD spectrum of the In:V = 1:1 film, in contrast, showed the presence of two crystalline phases: the prevailing monoclinic $InVO_4$-I (JCPDF 38-1135) phase with a grain size below 40 nm and the orthorhombic $InVO_4$-III (JCPDF 48-0898) phase. The structure of the monoclinic $InVO_4$-I phase [22] consists of compact In_4O_{16} groups of four edge-shared InO_6 octahedra. These In_4O_{16} groups are linked to each other by VO_4 tetrahedra. The structure of the orthorhombic $InVO_4$-III phase [23] is composed of chains of InO_6 octahedra which are linked together by VO_4 tetrahedra.

IR spectra of films

The IR spectra of the investigated $FeVO_4$, $InVO_4$, and $Fe_2V_4O_{13}$ films are presented in Figs. 7–9. The spectra of the films prepared at lower temperatures are characterized by broad bands which confirm the findings of the electron microscopic investigations (Figs. 1–5) – a dominating amorphous phase in which the nanograins are embedded. With increasing temperature the number of IR bands also increases, as does their sharpness. Thermal treatment at 500°C ($FeVO_4$, $InVO_4$) and 400°C ($Fe_2V_4O_{13}$) leads to the formation of crystalline films. For all

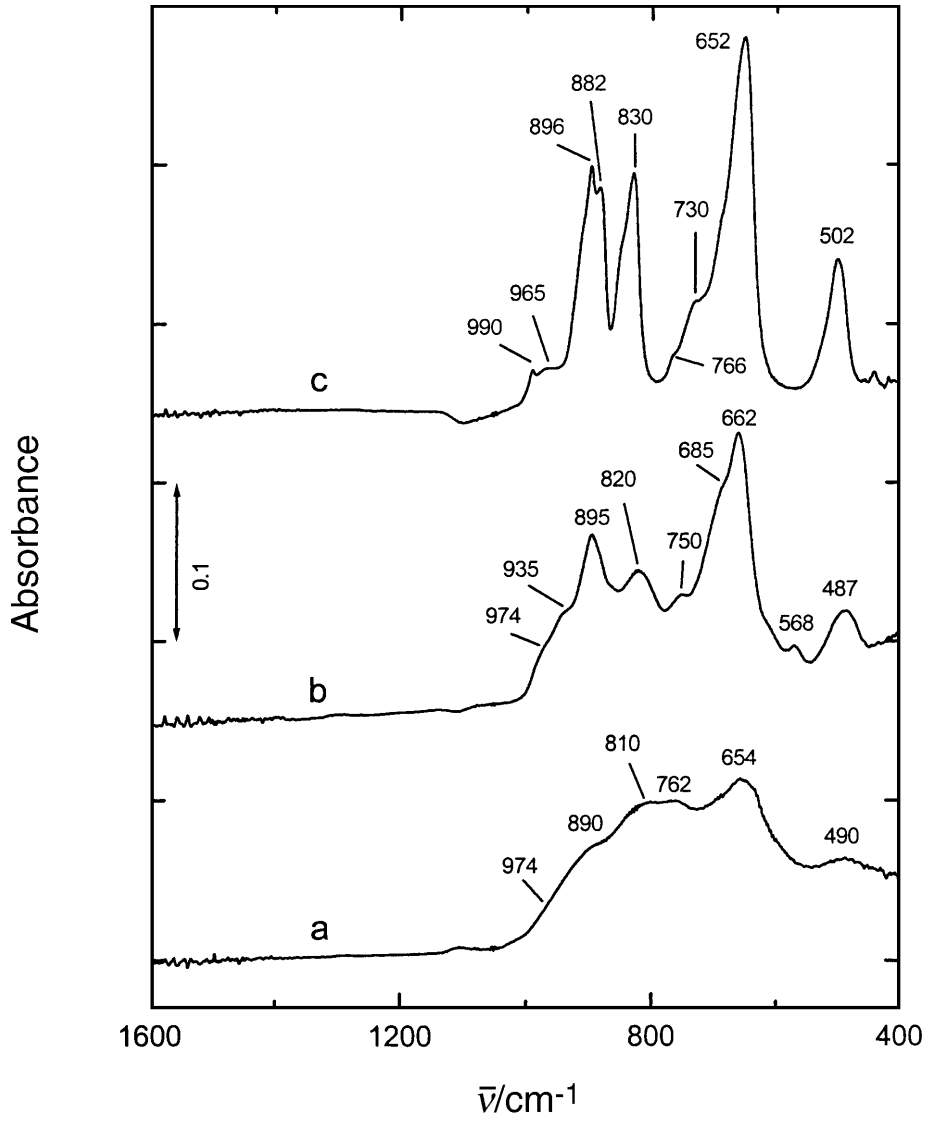

Fig. 7. IR absorbance spectra of $FeVO_4$ films thermally treated for 1 h at a) 300°C, b) 400°C, c) 500°C

investigated compounds the IR bands can be assigned to three or four major regions (Table 1) depending on their structure: V–O terminal stretching (1050 to $\sim 850\,cm^{-1}$), bridging V–O $\cdots M$ ($M =$ In, Fe), V $\cdots$ O $\cdots M$ and V–O–V stretching (~ 850 to $\sim 550\,cm^{-1}$), V–O–V deformation and Fe–O stretching ($< 550\,cm^{-1}$) [9–14, 26–29]. This assignment was made on the basis of the assignment of lead vanadate glasses according to *Hayakawa et al.* [26], who assumed that the glasses consist of $(VO_3)_n$ chains of corner-sharing VO_4 groups with V–O bonds of different strengths. In orthovanadates, VO_4 groups do not form chains among themselves and bridging V–O $\cdots$ Fe and V $\cdots$ O $\cdots$ Fe modes with stronger or weaker bonds appear in the region between 500 and $850\,cm^{-1}$. In contrast to $InVO_4$ and $FeVO_4$ orthovanadates, the bridging V–O–V stretching is present

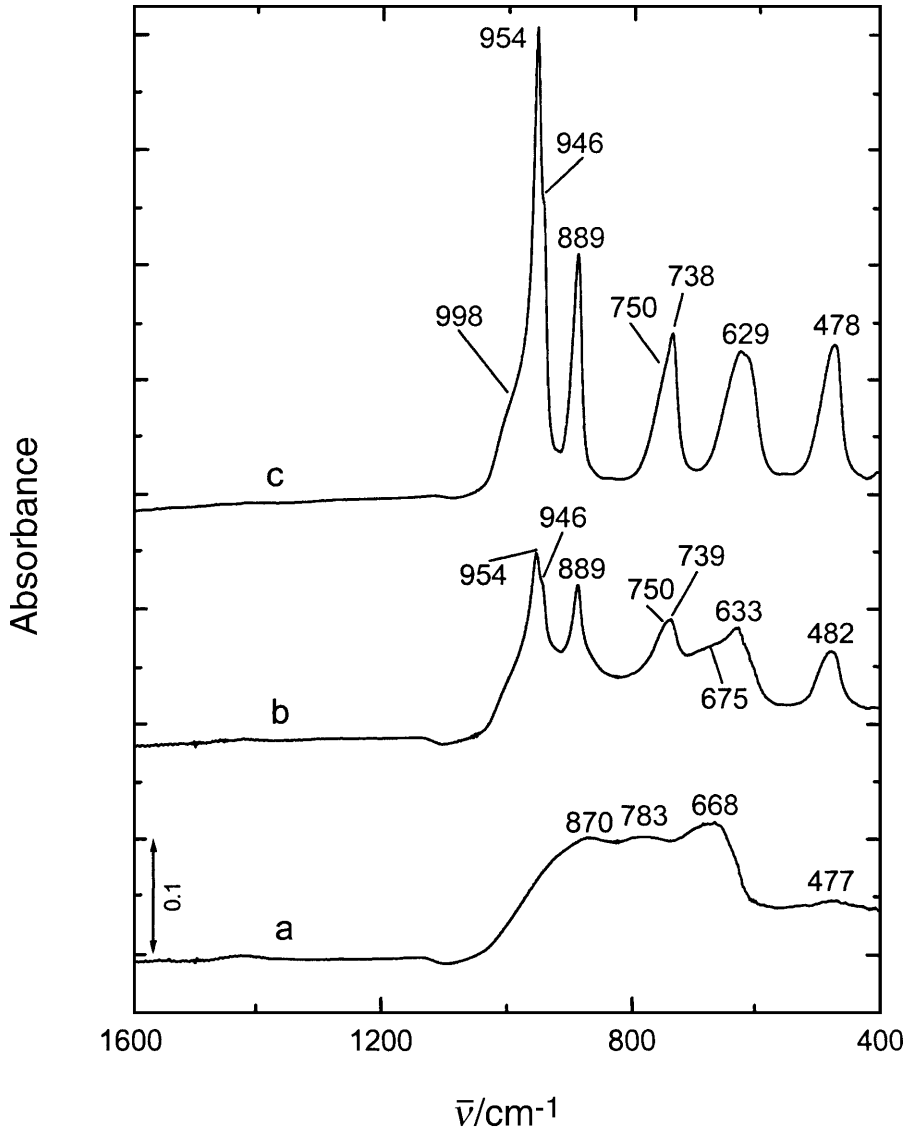

Fig. 8. IR absorbance spectra of $InVO_4$ films thermally treated for 1 h at a) 300°C, b) 400°C, c) 500°C

in the IR spectra of $Fe_2V_4O_{13}$ films due to the $(V_4O_{13})^{6-}$ anions in the crystalline structure [19].

VO_4^{3-} ions in aqueous solutions exhibit two IR active modes [30]: the totally symmetric (v_1, A symmetry) mode at 824 cm^{-1} and the asymmetric (v_3, F_3 symmetry) mode at 790 cm^{-1}. In condensed structures, due to the decrease in the site symmetry, the shift of the IR bands to higher frequencies and the splitting of the triply degenerated v_3 mode are expected. The symmetric v_1 stretching appears, for example, at 915 cm^{-1}, and the split v_3 modes at 890, 770, and 680 cm^{-1} for $InVO_4$ and $TlVO_4$ [28]. The presence of more than three separate bands in the v_3 stretching region indicates strong coupling between different VO_4 tetrahedra and M^{3+}–O (M = Fe, Al, Cr, ...) polyhedra in the unit cell. It is known, however, that

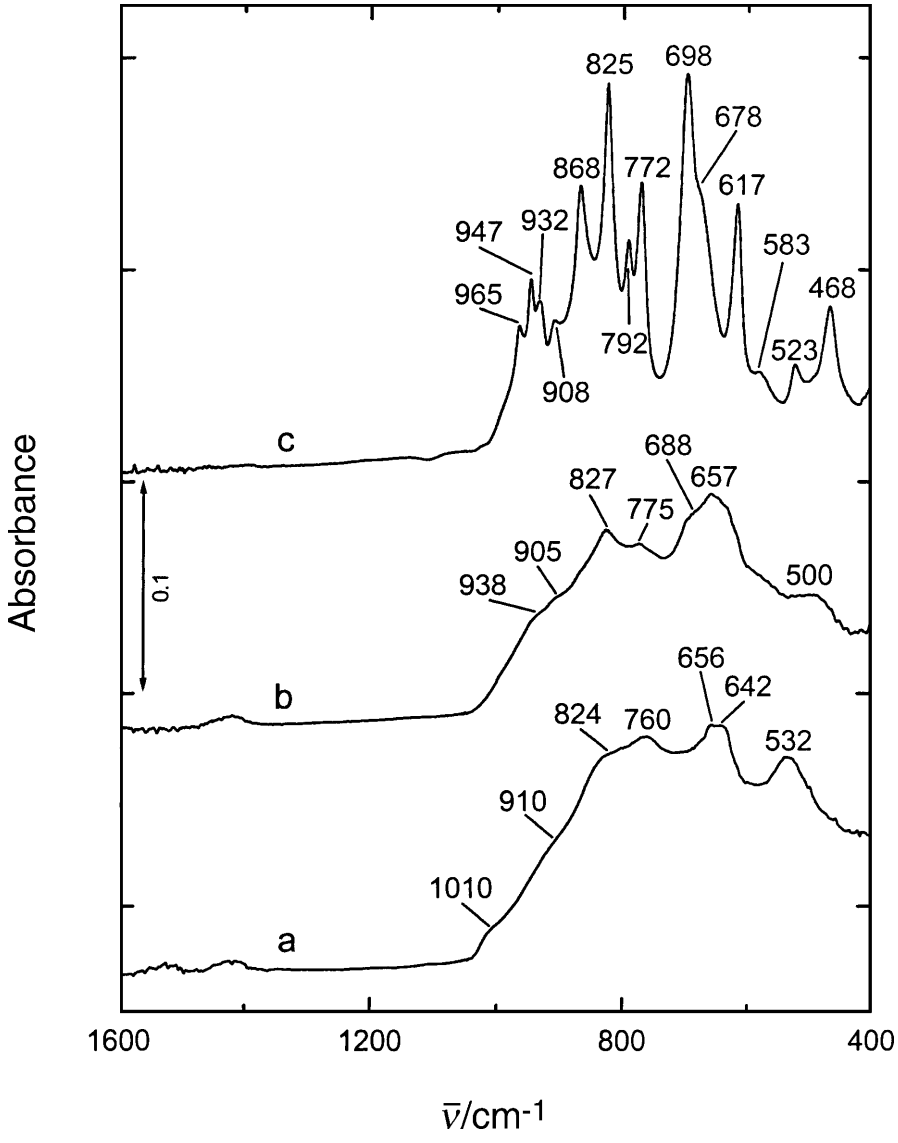

Fig. 9. IR absorbance spectra of $Fe_2V_4O_{13}$ films thermally treated for 1 h at a) 200°C, b) 300°C, c) 400°C

from pure V_2O_5 [25] to ortovanadates [20–23] a trend of longer chemical bonds and a lower coordination number of the vanadium with respect to the oxygen is observed [27]. In the IR spectra of the orthovanadates [28, 29] the intense bands around 1000 cm^{-1}, signifying the short isolated V=O bonds, are not formed. The symmetry of VO_4^{3-} groups in orthovanadates decreases due to condensation effects, resulting in an increase in the number of absorption bands in the IR spectra.

We can conclude that the crystallization of Fe–V–O and In–V–O films proceeds through different stages. In the first stage (temperature < 200°C), the structure consists of an amorphous phase with vanadium polyhedra and metal ions ($M =$ Fe, In) probably bonded on the interstitial sites (isolated V=O bonds) [27]. During the second stage ($\sim$300°C), nanograins with $FeVO_4$-II or $InVO_4$-III

Table 1. Assignment of IR bands (cm^{-1}) of $InVO_4$, $FeVO_4$, and $Fe_2V_4O_{13}$ films

Assignment	Range	300°C	400°C	500°C
$InVO_4$				
V–O terminal stretching	1000–850			998
			954	954
			946	946 sho (III)
		870	889	889
Bridging V–O···In stretching	850–700	783		
			750	750
			739	738
Brinding V···O···In stretching	700–550	668	675	
			633	629
V–O–V deformation	< 550	477	482	478
$FeVO_4$				
V–O terminal stretching	1050–880	974	974	990
		890	935	965
			895	896
				882
Bridging V–O···Fe stretching	880–700	810	820	830
		762	750	766
			685	730
Mixed bridging V–O···Fe and V···O···Fe stretchings	700–550	654	662	652
			568	
V–O–V deformation, Fe–O stretching	< 550	490	487	502
$Fe_2V_4O_{13}$				
V–O terminal stretching	1050–800	1010		965
				947
			938	932
		910	905	908
				868
		824	827	825
Mixed bridging V–O–V and V–O···Fe stretching	800–600			792
		760	775	772
			688	698
		656	657	678
		642		
				617
V–O–V deformation, Fe–O stretching	< 600			583
		532	500	523
				468

structure and dimensions of 1 nm (Fe:V = 1:2, In:V = 1:1) or 5 nm (Fe:V = 1:1) are formed. The outer parts of these nanograins are probably terminated with vanadium polyhedra. At higher temperatures (400 and 500°C) the films become

crystalline, but the dimensions of the grains are different (from below 40 nm to 80 nm).

Ex situ IR absorbance spectroelectrochemical measurements

With this study we wanted to generalize the IR spectroscopic behaviour of orthovanadate ($M^{3+}VO_4$, M = Fe, In) and vanadate ($Fe_2V_4O_{13}$) thin films that were thermally treated at high temperatures (500°C for orthovanadates, 400°C for $Fe_2V_4O_{13}$) during electrochemical cycling. Prior to *ex situ* IR absorbance measurements, the films were charged or discharged in 1 M $LiClO_4$ in propylene carbonate (*PC*) using chronopotentiometry (i = constant) or chronocoulometry (E = constant). Details of the electrochemical charging/discharging are described in Table 2. In Figs. 10–12 (curves a, b) we first present the spectra of $FeVO_4$, $InVO_4$, and $Fe_2V_4O_{13}$ films charged/discharged to -0.04 or $-0.06\,mC \cdot cm^{-2} \cdot nm^{-1}$, the charging range in which the intercalation/deintercalation reaction of Li^+ ions is reversible. The second pair of spectra in Figs. 10–12 (curves c, d) shows the IR spectra of highly charged/discharged films which indicate large structural changes and amorphization.

The basic question when interpreting the spectral changes of charged/discharged films is the assessment of interactions between the intercalated Li^+

Table 2. Intercalation properties of crystalline $InVO_4$, $FeVO_4$, and $Fe_2V_4O_{13}$ films during *ex situ* IR absorbance measurements

Film	T_h/°C	d/nm	Charging technique	E/V	$i/\mu A \cdot cm^{-2}$	t_c/s
$InVO_4$	500	230	CE	–	22.3	448
						1792
$FeVO_4$	500	90	CE	–	35.0	143
					32.1	936
$Fe_2V_4O_{13}$	400	70	CC	−1.50	–	120
				−3.00	–	480

Film	$Q_{ins}/mC \cdot cm^{-2}$	$Q_{ins} \cdot d^{-1}/mC \cdot cm^{-2} \cdot nm^{-1}$	$\rho/g \cdot cm^{-3}$	x	x'
$InVO_4$	−10.0	−0.04	4.61	0.23	–
	−40.0	−0.17		0.90	
$FeVO_4$	−5.0	−0.06	3.65	0.27	–
	−30.0	−0.33		1.62	
$Fe_2V_4O_{13}$	−4.3	−0.06	3.12	0.27	1.07
	−23.3	−0.33		1.44	5.77

T_h: temperature of thermal treatment; d: thickness of films; E: charging potential; i: current density; t_c: time of charging; Q_{ins}: charge density; $Q_{ins} \cdot d^{-1}$: charge density per film thickness; ρ: density of crystalline phases; x: intercalation coefficient per V atom; x': molar ratio of Li in $Li_xFe_2V_4O_{13}$; all films were thermally treated for 1 h; charging/discharging was performed using chronopotentiometry (CE) or chronocoulometry (CC)

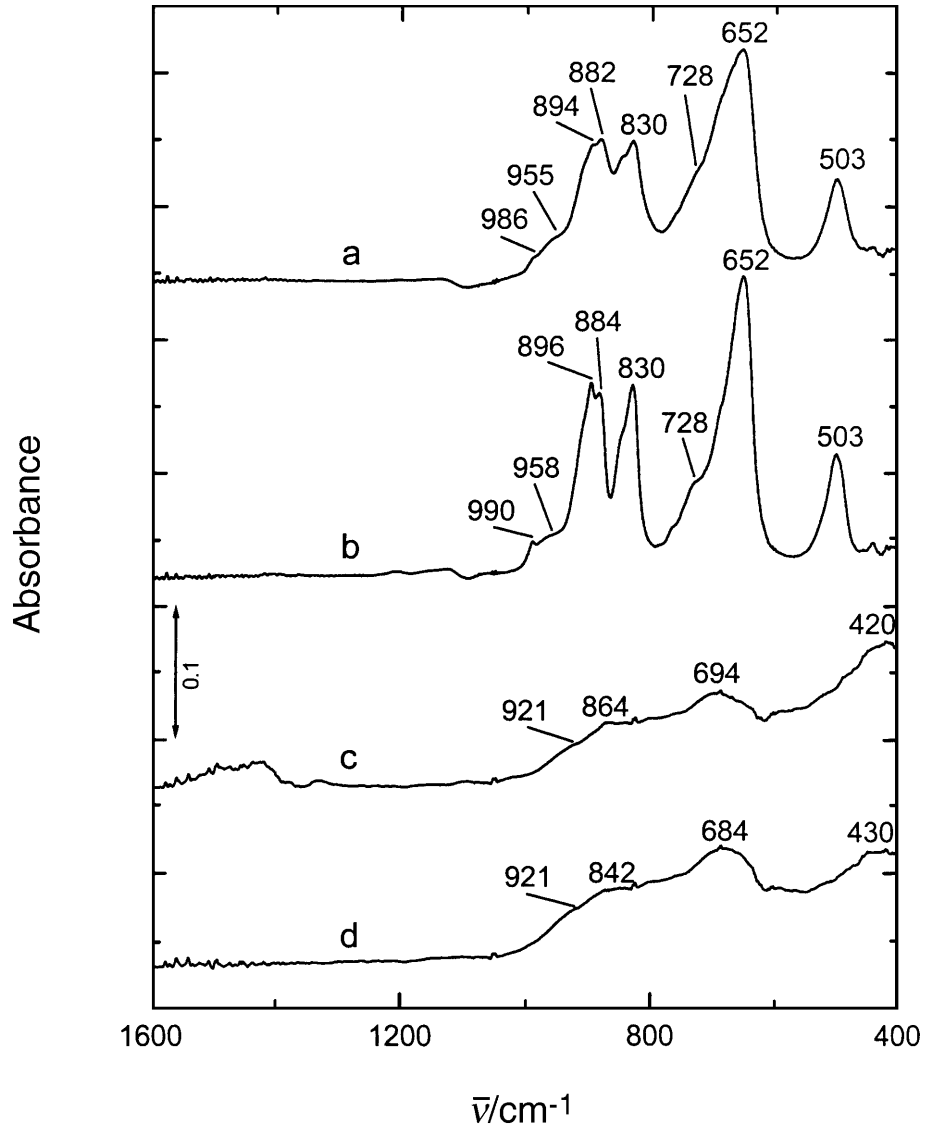

Fig. 10. *Ex situ* IR absorbance spectra of a $FeVO_4$ film (500°C, 1 h): a) charged to $-0.06\,mC \cdot cm^{-2} \cdot nm^{-1}$, b) discharged from $-0.06\,mC \cdot cm^{-2} \cdot nm^{-1}$, c) charged to $-0.33\,mC \cdot cm^{-2} \cdot nm^{-1}$, d) discharged from $-0.33\,mC \cdot cm^{-2} \cdot nm^{-1}$

ions and the film network. The strength of interactions is responsible either for only small changes in the film structure or for the amorphization of the structure. In the former case, the structural change is topotactic, and the atoms return to their original positions after discharging. For amorphous films, IR spectroscopy is a powerful technique for obtaining information about the groups of atoms that change their redox state or about the atoms that interact with the inserted Li^+ ions. Without having the results of the normal coordinate treatment at hand (rarely available for vanadates [28]), the electrochemically induced changes in films can be explained at least quantitatively by comparing the IR spectra of films in initial, intercalated, and deintercalated states to the spectra of model compounds.

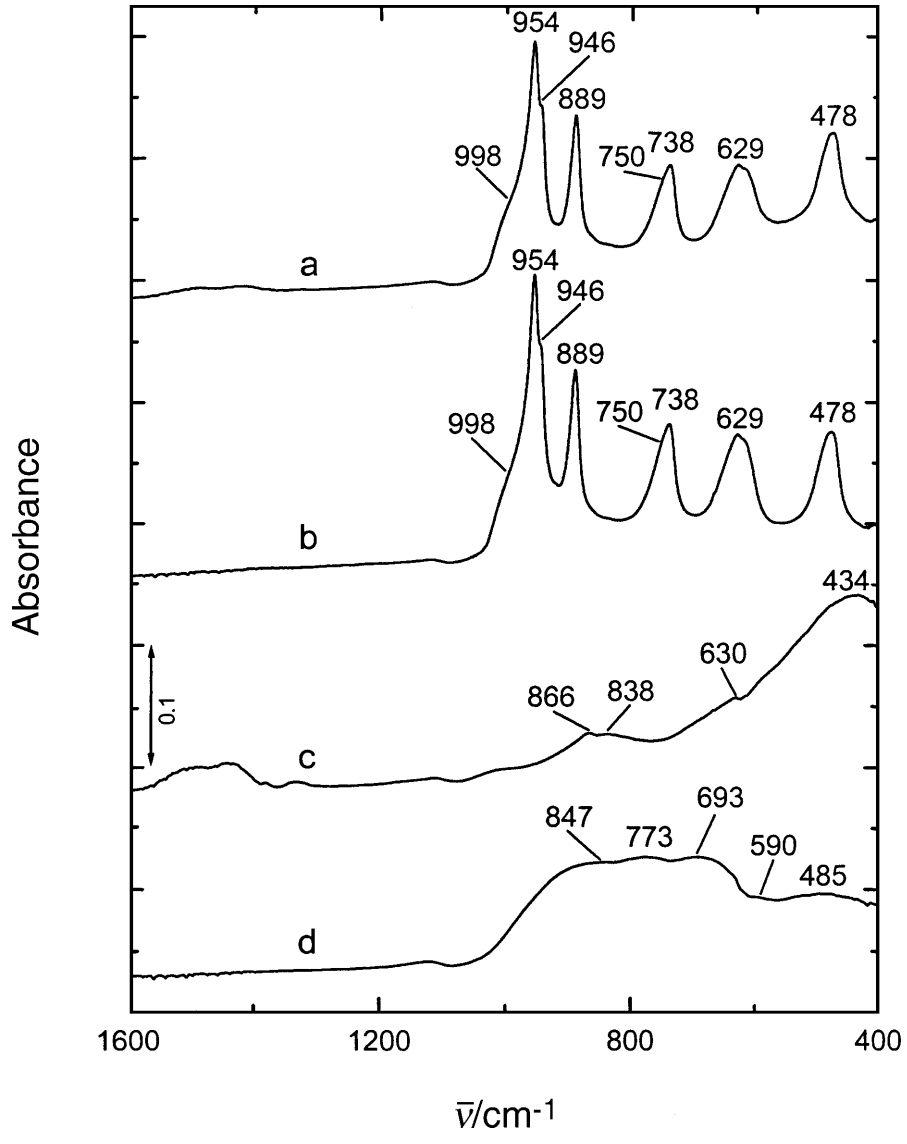

Fig. 11. *Ex situ* IR absorbance spectra of an $InVO_4$ film (500°C, 1 h): a) charged to $-0.04\ mC \cdot cm^{-2} \cdot nm^{-1}$, b) discharged from $-0.04\ mC \cdot cm^{-2} \cdot nm^{-1}$, c) charged to $-0.17\ mC \cdot cm^{-2} \cdot nm^{-1}$, d) discharged from $-0.17\ mC \cdot cm^{-2} \cdot nm^{-1}$

It is clear from curves a and b in Figs. 10–12 that small inserted charges lead to a decrease in the intensity of the IR bands, whereas their positions remain almost unaltered. In the spectra of charged films (Figs. 10–12a) an increase in the background absorption is also observed, and this is most evident for the $InVO_4$ film (Fig. 11a). This effect was ascribed to Li^+–O stretching, since these modes are expected in the spectral region below $600\ cm^{-1}$. Previous IR spectroscopic studies [31, 32] also have shown that only the tetrahedrally coordinated Li^+ ions give rise to the IR bands between 400 and $600\ cm^{-1}$. After discharging (Figs. 10–12b) we detected spectra very similar to those of the initial films; this confirmed the

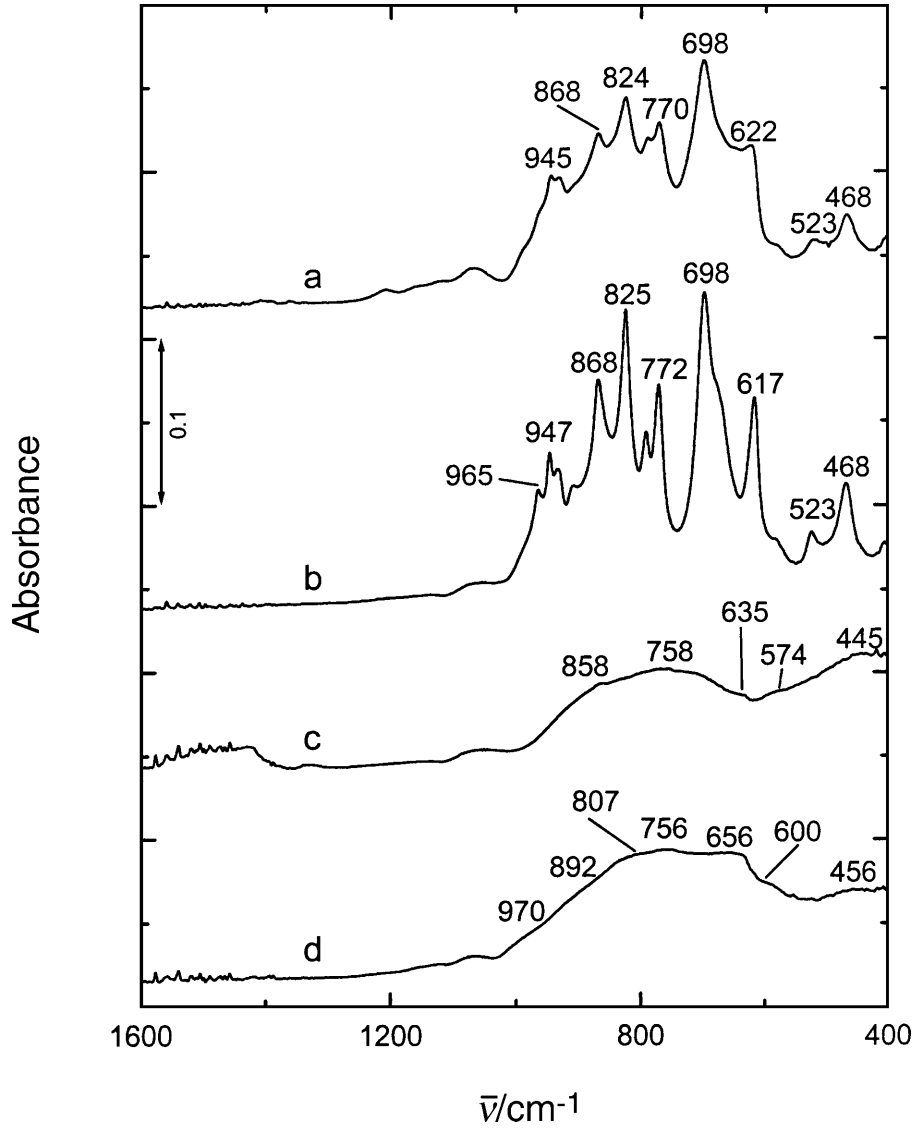

Fig. 12. *Ex situ* IR absorbance spectra of an $Fe_2V_4O_{13}$ film (400 °C, 1 h): a) charged to $-0.06\,mC \cdot cm^{-2} \cdot nm^{-1}$, b) discharged from $-0.06\,mC \cdot cm^{-2} \cdot nm^{-1}$, c) charged to $-0.33\,mC \cdot cm^{-2} \cdot nm^{-1}$, d) discharged from $-0.33\,mC \cdot cm^{-2} \cdot nm^{-}$

reversibility of the intercalation reaction. The background absorption was no longer visible.

A completely different situation was found for high chargings (Figs. 10–12c). Strong skeletal modes between 500 and 1000 cm^{-1} diminished in intensity and were substituted by broad bands with much lower intensities. On the other hand, a new and quite intense band appeared below 500 cm^{-1} and was superimposed on the background absorption. This band could be ascribed to the V–O–V (in the case of $Fe_2V_4O_{13}$) or V–O $\cdots$ M^{3+} (M = In, Fe) bridging stretching vibrations of vanadium in the reduced state ($4+$ or $4+/3+$). Alternatively, it can be partly, together with the increase in the background absorption, attributed to the Li^+–O interactions.

Discharging led to IR spectra (Figs. 10–12d) that were quite similar to the IR spectra of the Fe–V–O and In–V–O films thermally treated at lower temperatures (300°C) shown in Figs. 7–9. This similarity is more noticeable for both orthovanadate films than for the $Fe_2V_4O_{13}$ films: the intensities of the bands are similar, whereas the band frequencies are changed to a small extent. The similarity of the IR spectra shows that the amorphization occurred in initially crystalline films after high discharging. The amorphization is, however, not complete, and the appearance of the IR bands suggets that the nanograins remained in the highly discharged films. In the spectra of discharged orthovanadate films we also observed an increased intensity below 600 cm^{-1} compared to the spectra of the initial low-temperature films. This increase in intensity showed that the charging/discharging

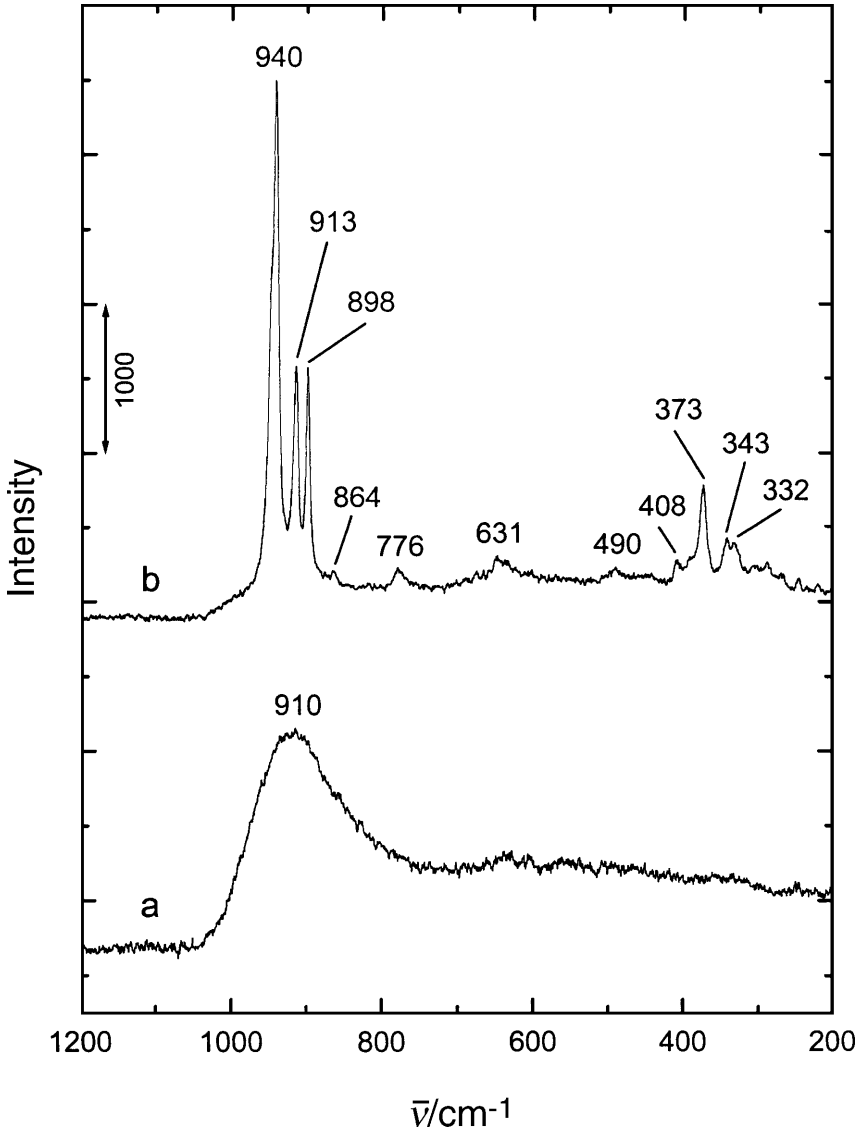

Fig. 13. *Raman* spectra of $InVO_4$ films thermally treated for 1 h at a) 300°C, b) 500°C

reaction is no longer reversible, but that the amorphisized films remain irreversibly lithiated.

Raman spectroscopy provided interesting results in the case of $InVO_4$ films. In Fig. 13, the *Raman* spectra of initial $InVO_4$ films prepared at 300 and 500°C are presented. The former spectrum has, in the skeletal region, a broad and diffuse V–O stretching band at 910 cm^{-1} (Fig. 13a). The rather large bandwidths indicate a large short-range disorder which can be due to the distribution of bond lengths and vacancies. The *Raman* spectrum of the $InVO_4$ film prepared at 500°C reveals bands at 960 (shoulder), 940, 913, and 898 cm^{-1} in the V–O stretching region. The

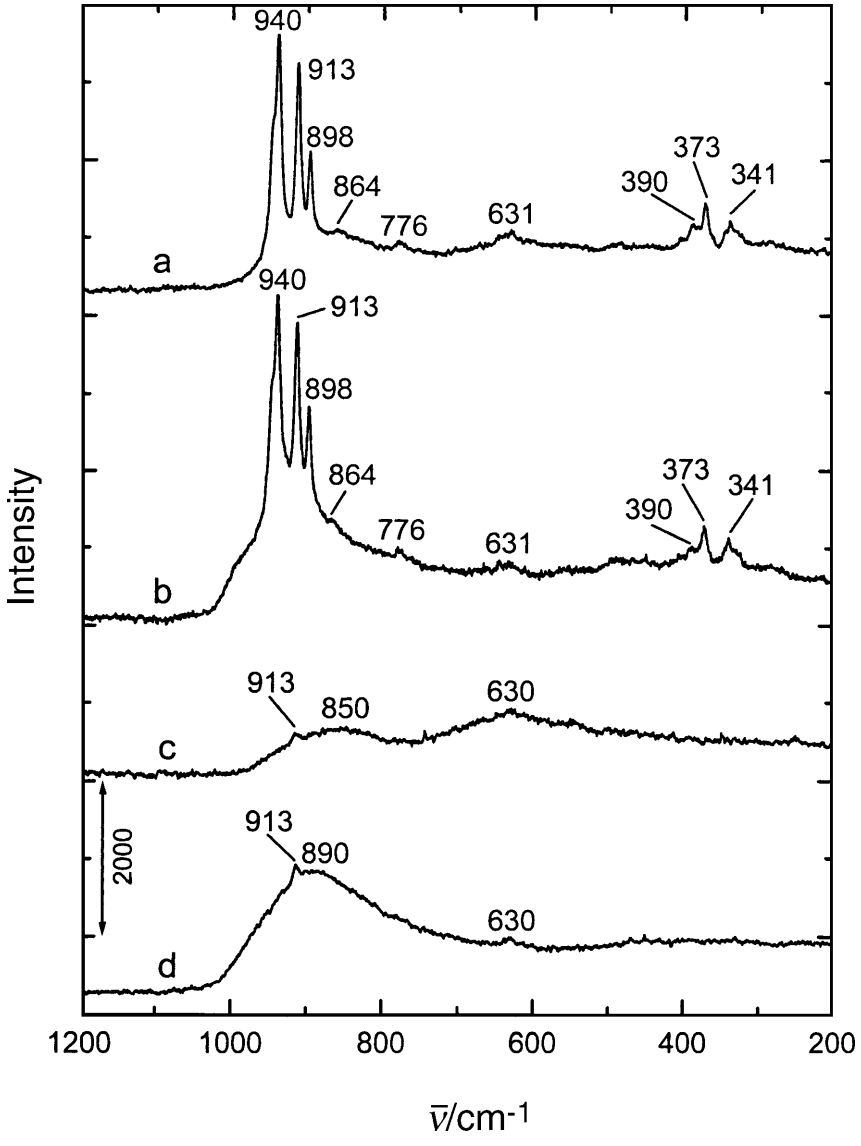

Fig. 14. *Ex situ Raman* spectra of an $InVO_4$ film (500°C, 1 h): a) charged to $-0.09\,mC \cdot cm^{-2} \cdot nm^{-1}$ ($x = 0.45$), b) discharged from $-0.09\,mC \cdot cm^{-2} \cdot nm^{-1}$, c) charged to $-0.17\,mC \cdot cm^{-2} \cdot nm^{-1}$ ($x = 0.90$), d) discharged from $-0.17\,mC \cdot cm^{-2} \cdot nm^{-1}$

913 cm^{-1} band [28] indicates the presence of the orthorhombic $InVO_4$-III phase, whereas the other bands belong to the monoclinic $InVO_4$-I phase. The exact amount of orthorhombic $InVO_4$-III is difficult to assess, but from the intensity of the 913 cm^{-1} band it is certainly less than 20%.

The assignment of the 913 cm^{-1} band to the orthorhombic phase was confirmed by *ex situ Raman* spectroelectrochemical measurements (Fig. 14). The $InVO_4$-I and the $InVO_4$-III phases exhibit different electrochemical behaviour [1]: the monoclinic phase becomes electrochemically active at 1.9 V *vs*. Li (−1.4 V *vs*. Ag/AgCl), whereas the orthorhombic phase requires 0.9 V *vs*. Li (−2.4 V *vs*. Ag/AgCl). Therefore, the *ex situ Raman* spectrum of the film charged to $-0.09\ mC \cdot cm^{-2} \cdot nm^{-1}$ ($x = 0.45$) revealed a drop in the intensity of the bands of the monoclinic $InVO_4$-I phase as regards the 913 cm^{-1} band of the orthorhombic $InVO_4$-III phase (Fig. 14a).

The 913 cm^{-1} band is also present in the *Raman* spectra of the film charged/discharged to $-0.17\ mC \cdot cm^{-1} \cdot nm^{-1}$ ($x = 0.90$), indicating the presence of the orthorhombic phase (Fig. 14a,b). The intensity of this band is, however, significantly reduced when compared to its intensity in the *Raman* spectrum of the initial film (Fig. 13b). In contrast, the transformation of the monoclinic $InVO_4$-I phase is reflected in the appearance of the broad and low-intensity bands at 850 and 630 cm^{-1} in the spectrum of the charged film (Fig. 14c). After discharging, the V–O stretching mode shifts to 890 cm^{-1} (Fig. 14d). The shift of the V–O stretching mode to lower wave numbers with charging was also observed in the IR spectra of charged crystalline V_2O_5 films [33] and is typical for Li^+–O interactions.

We can conclude that up to a potential of 1.7 V *vs*. Li, the range where SnO_2/F electrodes are stable, only the monoclinic $InVO_4$-I phase changes its crystalline structure to amorphous. The amorphization of the orthorhombic phase was not expected in the potential range used, and the 913 cm^{-1} band – although having lower intensity – is clearly seen in the highly discharged films (Fig. 14d). These results unambiguously show the structural similarity of highly discharged films and films prepared at lower temperatures (300°C).

Experimental

Preparation of thin films

Vanadate films were prepared using the sol-gel technique. For In–V–O films, $In(NO_3)_3 \cdot 5H_2O$ was first dissolved in *n*-propanol. To this solution V-oxoisopropoxide was added so that the molar ratio in the precursors was 1:1. A yellow-orange sol suitable for a dip coating deposition was obtained. We also used the same procedure for the preparation of Fe/V sols. The precursors $Fe(NO_3)_3 \cdot 9H_2O$ and V-oxoisopropoxide were mixed in *n*-propanol in molar ratios of Fe:V = 1:1 and 1:2 which resulted in dark-red sols. All films were deposited by dip coating with a pulling velocity of 10 $cm \cdot min^{-1}$ and then thermally treated at 300, 400, and 500°C for 1 h.

Instruments and measuring techniques

To determine the film thickness we used a Profilometer Talysurf (Taylor Hobson). IR absorbance spectra of the films were measured using a Perkin Elmer System 2000 with a resolution of 4 cm^{-1}. For these measurements the films were deposited on double-sided polished Si wafers with an electrical resistivity of 10–20 ohm · cm and partly transparent to IR radiation (∼50%). An In–Ga

alloy was used to improve the electrical contact. *Ex situ* IR spectra were measured after charging/discharging of the films with either chronopotentiometry (constant current density) or chronocoulometry (constant potential) on an EG&G Par 273 potentiostat/galvanostat. In a three-electrode electrochemical cell the film was connected as a working electrode; a Pt rod was connected as a counter electrode, and a modified Ag/AgCl electrode, was used as a reference.

For *Raman* measurements, all films were deposited on SnO_2/F glass substrates. The *ex situ Raman* spectra were measured on an XY spectrograph (Dilor, France) equipped with a double monochromator as a filter and a back-illuminated liquid nitrogen-cooled 2000×800 pixels charge-coupled device detector (Spex, a division of the Jobin-Yvone company, France).

Samples were examined using analytical electron microscopy (AEM) in both directions: parallel (plan view) and perpendicular (cross section) to the thin film. A cross section of the Fe–V–O samples (400 and 500°C) on a ⟨Si⟩ substrate was prepared using a Gatan cross-sectional TEM specimen preparation kit. After mechanical thinning and dimpling, the samples were ion milled using 3.8 keV argon ions. To prevent degradation the sample was cooled with liquid nitrogen during the final stages of the ion erosion process. Samples were examined using a JEOL 2000 FX transmission electron microscope operating at 200 kV. The chemical composition of the phases was determined using a Link AN-1000 energy-dispersive X-ray spectroscopy (EDXS) system with an ultra-thin window Si(Li) detector. Fragments of the thin Fe–V–O film, fired at 300°C, were prepared by gentle scratching of the film's surface and subsequent transfer to a hollow carbon-coated Cu grid for AEM examination.

References

[1] Denis S, Baudrin E, Touboul M, Tarascon J-M (1997) J Electrochem Soc **144**: 4099
[2] Hayashibara M, Eguchi M, Miura T, Kishi T (1997) Solid State Ionics **98**: 119
[3] Sugawara M, Fujiwara M, Matsuki K (1993) Denki Kagaku **61**: 224
[4] Picardi G, Varsano F, Decker F, Opara Krašovec U, Šurca A, Orel B (1999) Electrochim Acta **44**: 3157
[5] Opara Krašovec U, Orel B, Reisfeld R (1998) Electrochem Solid-State Lett **1**: 104
[6] Opara Krašovec U, Orel B, Šurca A, Bukovec N, Reisfeld R (1999) Solid State Ionics **118**: 195
[7] Granqvist CG (1995) Handbook of Inorganic Electrochromic Materials. Elsevier, Amsterdam
[8] Cocciantelli JM, Doumerc JP, Pouchard M, Broussely M, Labat J (1991) J Power Sources **34**: 103
[9] Benčič S, Orel B, Šurca A, Lavrenčič Štangar U (2000) Solar Energy **68**: 499
[10] Šurca A, Orel B, Opara Krašovec U, Lavrenčič Štangar U, Dražič G (2000) J Electrochem Soc **147**: 2358
[11] Orel B, Šurca Vuk A, Opara Krašovec U, Dražič G (2001) Electrochim Acta **46**: 2059
[12] Šurca Vuk A, Opara Krašovec U, Orel B, Colomban P (2001) J Electrochem Soc **148**: H49
[13] Šurca Vuk A, Orel B, Dražič G, Decker F, Colomban P (2001) Sol-Gel Science and Technology **23**
[14] Šurca Vuk A, Orel B, Dražič G (2001) Journal of Solid State Electrochemistry **5**: 437
[15] Williams DB, Carter CB (1996) Transmission Electron Microscopy – Part II: Diffraction. Plenum, New York, p 274
[16] Rudee ML, Howie A (1972) Phil Mag **25**: 1001
[17] Graczyk JF, Chaudahari P (1973) Phys Status Solidi b **58**: 163
[18] Stadelmann PA (1987) Ultramicroscopy **21**: 131
[19] Permer L, Laligant Y (1997) Eur J Solid State Inorg Chem **34**: 41
[20] Robertson B, Kostiner E (1972) J Solid State Chem **4**: 29
[21] Oka Y, Yao T, Yamamoto N, Ueda Y, Kawasaki S, Azuma M, Tanako M (1996) J Solid State Chem **123**: 54
[22] Touboul M, Melghit K, Bénard P, Louër D (1995) J Solid State Chem **118**: 93
[23] Touboul M, Tolédano P (1980) Acta Cryst B **36**: 240

[24] Blake RL, Hessevick RE Yoltai T, Finger LW (1966) American Mineralogist **51**: 123
[25] Enjalbert R, Galy J (1986) Acta Cryst C **42**: 1467
[26] Hayakawa S, Yoko T, Sakka S (1995) J Non-Cryst Solids **183**: 73
[27] Dimitriev Y, Dimitrov V, Arnaudov M, Topalov D (1983) J Non-Cryst Solids **57**: 147
[28] Baran EJ, Escobar ME (1985) Spectrochim Acta **41**: 415
[29] Roncaglia DI, Botto IL, Baran EJ (1986) J Solid State Chemistry **62**: 11
[30] Müller A, Baran EJ, Hendra PJ (1969) Spectrochim Acta **25A**: 1654
[31] Tarte P (1962) Spectrochim Acta **18**: 467
[32] Tarte P (1964) Spectrochim Acta **20**: 238
[33] Šurca A, Orel B, Dražič G, Pihlar B (1999) J Electrochem Soc **146**: 232

Received October 4, 2001. Accepted (revised) November 23, 2001